A&A, 687, A137 (2024)
https://doi.org/10.1051/0004-6361/202348819


Astronomy & Astrophysics

# Radio properties of green pea galaxies

A. Borkar[1], R. Grossová[1,2], J. Svoboda[1], E. Moravec[3], K. Kouroumpatzakis[1], P. G. Boorman[4], B. Adamcová[1], B. Mingo[5], and M. Ehle[6]

[1] Astronomical Institute of the Czech Academy of Sciences, Boční II 1401, 14100 Prague, Czech Republic
e-mail: borkar@asu.cas.cz
[2] Department of Theoretical Physics and Astrophysics, Faculty of Science, Masaryk University, Kotlářská 2, Brno 61137, Czech Republic
[3] Green Bank Observatory, PO Box 2, Green Bank, WV 24944, USA
[4] Cahill Center for Astronomy and Astrophysics, California Institute of Technology, Pasadena, CA 91125, USA
[5] School of Physical Sciences, The Open University, Walton Hall, Milton Keynes MK7 6AA, UK
[6] European Space Agency, European Space Astronomy Centre (ESA/ESAC), Camino Bajo del Castillo s/n, 28692 Villanueva de la Cañada, Madrid, Spain

Received 1 December 2023 / Accepted 29 March 2024

**ABSTRACT**

*Aims.* Green peas (GPs) are young, compact, star-forming dwarf galaxies, and local ($z \sim 0.3$) analogues of the early galaxies ($z \geq 6$) considered to be mainly responsible for the reionisation of the Universe. Recent X-ray observations of GPs led to the detection of high excess emission, which cannot be accounted for by star formation alone and implies the presence of an active galactic nucleus (AGN). We employ radio observations to study the radio properties of GPs, build their radio spectral energy distributions, and verify the presence of AGNs.

*Methods.* We performed new radio observations of three GPs with the *Karl G. Jansky* Very Large Array (JVLA) in the *L*, *C*, and *X* bands (1.4, 6 and 10 GHz resp.), and analysed them alongside data from archival observations and large radio surveys. We also analysed the archival radio data for a larger sample of GPs and blueberry (BBs) galaxies, which are lower-mass and lower-redshift analogues of the GPs. To understand the significance of the radio observations, we assess the detectability of these sources, and compare the detected radio luminosities with expectations from theoretical and empirical relations.

*Results.* Two of the three targeted GPs are strongly detected ($>10\sigma$) in the JVLA observations and their fluxes are consistent with star formation, while the third source is undetected. Although archival radio surveys have the sensitivity to detect a large fraction (~75%) of the sources from the larger archival sample of GPs and BBs, we only detect a small number (<40%) of them and their radio luminosity is significantly lower than the expectation from empirical relations.

*Conclusions.* Our results show that the majority of the dwarf galaxies in our sample are highly underluminous. The radio luminosity–star formation rate (SFR) relation deviates from the empirical relations, especially towards the lower end of galaxy mass and SFR, suggesting that the relations established for larger galaxies may not hold towards the low-mass end.

**Key words.** galaxies: dwarf – galaxies: starburst – galaxies: star formation – radio continuum: galaxies

## 1. Introduction

In the hierarchical formation model, larger galaxies ($\log(M_\star/M_\odot) \geq 10$) observed at low redshift are formed through continuous mergers of smaller galaxies (see e.g. Cole et al. 2000). The first galaxies were young, low-mass (dwarf, $\log(M_\star/M_\odot) < 9.5$) sources and were likely the hosts of the first generation of stars which were responsible for the reionisation of the Universe, when the neutral gas was almost completely ionised. This epoch of reionisation ($6 < z < 20$; Bouwens et al. 2015; Robertson et al. 2015) is pivotal to our understanding of cosmology and structure formation. The dwarf galaxies present at this epoch are characterised by their low mass, vigorous star formation and relatively low metallicity, and their production of a vast amount of ultraviolet (UV) and Lyman continuum radiation from young, massive stars, which can ionise hydrogen atoms in the intergalactic medium (Steidel et al. 2001). The intense star formation in these early galaxies has long been thought to be the main cause of cosmic reionisation (Shapiro & Giroux 1987; Loeb & Barkana 2001). Quasars and AGNs, which are powered by accretion onto supermassive black holes could also provide the necessary photons for reionisation. The relative proportions of the contribution of star formation and AGN emission to cosmic reionisation are still a matter of debate, and some studies suggest that the AGN emission could substantially contribute to the reionisation (Volonteri & Gnedin 2009; Giallongo et al. 2015).

Until recently, these early galaxies were difficult to observe because of their high redshift, as the UV-optical emission from star formation has been shifted to the infrared (IR) band, which is unreachable with ground-based observatories and the limited sensitivity of space observatories. With the advent of JWST, redshifts beyond $z > 7$ have become accessible (see e.g. Naidu et al. 2022; Castellano et al. 2022; Finkelstein et al. 2022; Adams et al. 2023; Atek et al. 2023a,b; Labbé et al. 2023). Some of these galaxies seem to be hosting AGNs (Juodžbalis et al. 2023; Bogdán et al. 2024; Goulding et al. 2023). Although the JWST will uncover many high-$z$ dwarf galaxies, studying them in detail is challenging as it requires long exposures, which may not be achievable for

**Table 1.** Properties of the sample of GPs.

| Source name | SDSS name | RA [h:m:s] | Dec [d:m:s] | $z$ | $M_\star$ [log $M_\odot$] | SFR [$M_\odot\,\mathrm{yr}^{-1}$] | log $L_X$ [erg $\mathrm{s}^{-1}$] |
|---|---|---|---|---|---|---|---|
| GP1 | J074936.77+333716.3 | 07:49:36.773 | +33:37:16.395 | 0.2733 | 9.8 | 58.8 | 42.08 |
| GP2 | J082247.66+224144.0 | 08:22:47.672 | +22:41:44.101 | 0.2163 | 9.6 | 37.4 | 42.07 |
| GP3 | J133928.30+151642.1 | 13:39:28.309 | +15:16:42.022 | 0.1920 | 9.3 | 18.8 | <41.11 |

multi-wavelength observations. Thus, to obtain a holistic understanding of the physical processes in the galaxies responsible for cosmic reionisation, it is crucial to study their low-$z$ analogues with multi-wavelength observations, which can be achieved with the current generation of ground-based and space observatories.

Green pea galaxies (GPs) are a class of low-redshift ($z \sim 0.3$) galaxies discovered in the Sloan Digital Sky Survey (SDSS) Galaxy Zoo project (Cardamone et al. 2009). GPs are compact ($\leq$5 kpc), with a low stellar mass ($\log(M_\star/M_\odot) \sim 9$), and have a high star formation rate (SFR $\sim 10\,M_\odot\,\mathrm{yr}^{-1}$), and consequently a very high specific SFR (defined as the ratio of galaxy stellar mass and SFR: sSFR $= M_\star/\mathrm{SFR} \sim 10^{-8}\,\mathrm{yr}^{-1}$), and subsolar metallicities ($12 + \log[\mathrm{O/H}] < 8.7$). Strong Lyman-$\alpha$ lines are detected in a large fraction of GPs, and these show similarities with the high-redshift compact star forming galaxies called the Lyman alpha emitters (LAEs, Hayes 2015; Yang et al. 2017a). These similarities with the high-$z$ galaxies make the GPs ideal analogues with which to study the nature of the ionising radiation in detail (Schaerer et al. 2022; Rhoads et al. 2023).

Since the discovery of GPs, a few local ($z < 0.1$) samples of GP-like dwarf galaxies have been presented in the literature. Yang et al. (2017b) presented a sample of GP analogues ($z < 0.05$), called "blueberries" (BBs), with much lower stellar masses ($\log(M_\star/M_\odot) \approx 6.5$–$7.5$) and lower metallicities ($7.1 < 12 + \log(\mathrm{O/H}) < 7.8$) but with an sSFR similar to or higher than those of GPs. This latter sample was selected using SDSS imaging and photometry, along with compactness and large equivalent widths of optical emission lines. A similar sample was presented by McKinney et al. (2019) and Jaskot et al. (2019), who focused their selection on galaxies with the highest ionisation levels (high O III/O II line ratio). We refer to galaxies from both these samples as "blueberries" for simplicity.

Svoboda et al. (2019) reported the first X-ray observations of three GPs, based on *XMM-Newton* observations. These GPs were selected from the Cardamone et al. (2009) sample of 80 sources, which were classified as purely star forming galaxies in the Baldwin–Phillips–Terlevich (BPT) diagram (Baldwin et al. 1981), which had high SFR and lower redshift in order to facilitate favourable observability with *XMM-Newton*. These three selected sources are referred to by Svoboda et al. (2019) as GP1, GP2 and GP3[1]. The targeted sources are at redshift $z = 0.19$–$0.27$ and have high SFR of $\sim$20–60 $M_\odot\,\mathrm{yr}^{-1}$. Their stellar masses ($\log(M_\star/M_\odot) = 9.3$–$9.8$) and metallicities ($12 + \log(\mathrm{O/H}) = 8.1$–$8.3$) are slightly above average compared to the parent sample. The details of the three sources are in Table 1.

The X-ray observations with *XMM-Newton* led to the detection of extreme X-ray luminosities for star forming galaxies of namely $L_{2-10\,\mathrm{keV}} \sim 10^{42}\,\mathrm{erg\,s}^{-1}$, in two of the three targets (GP1 and GP2), a factor of >5 greater than the estimated luminosity from theoretical or empirical relations for star forming galaxies of similar mass range (see Svoboda et al. 2019 for the details). At the same time, the third target, GP3, was entirely undetected, even in the deeper follow-up observations. In the BPT diagram (Baldwin et al. 1981), GP1 is classified as strictly star forming, while GP2 and GP3 show line ratios that are on the border between the AGN-like and star forming classification (Cardamone et al. 2009). The observed excess X-ray emission in the two GPs seemingly cannot not be explained by a higher efficiency of high-mass X-ray binaries in the low-metallicity environment (Svoboda et al. 2019) or contributions from hot gas (Franeck et al. 2022), and implies the presence of an AGN.

A sizable fraction (>10–30%) of dwarf galaxies are expected to host AGNs (Miller et al. 2015; Kaviraj et al. 2019; Reines 2022). Radio observations provide a unique avenue in the search for AGNs in dwarf galaxies, as radio emission can probe black holes accreting at low Eddington ratios, while the optical tracers tend to select more highly accreting sources in low-SFR galaxies (Körding et al. 2006; Best & Heckman 2012; Moravec et al. 2022). Recently, several AGN candidate sources were detected in dwarf galaxies using radio observations (Nyland et al. 2012; Reines et al. 2014, 2020; Latimer et al. 2019; Mezcua et al. 2019). Radio observations also provide an independent way of estimating the SFR in these galaxies. Motivated by these detections, we proposed targeted observations of the three GPs with JVLA.

In the present paper, we provide the results of our dedicated JVLA observations of the three GPs, along with an analysis of the archival radio data for three GPs. We also explore the radio properties of the full GP sample from Cardamone et al. (2009) and the BB sample from Yang et al. (2017b) and Jaskot et al. (2019) as a comparison. The paper is arranged in the following way: In Sect. 2, we present the details of the JVLA observations, data reduction and the observational results. Further, we present the compilation of the archival radio data for the targeted GPs and the samples of dwarf galaxies. We compare the radio observations of our targeted GPs with the comparison sample in Sect. 3. In Sect. 4, we explore the relation between star formation and radio flux in dwarf galaxies and its implications for observations of GPs. The main conclusions are summarised in Sect. 5. We use the following cosmological parameters: $H_0 = 67.7\,\mathrm{km\,s}^{-1}\,\mathrm{Mpc}^{-1}$, $\Omega_M = 0.31$, and $\Omega_\Lambda = 0.69$ (Planck Collaboration VI 2020). For radio spectral index $\alpha$, we use the convention $S_\nu \propto \nu^\alpha$.

## 2. Radio data analysis

### 2.1. JVLA observations

We selected the three GPs with X-ray observations from Svoboda et al. (2019) for targeted JVLA observations (ID: VLA/21B-136, PI: A. Borkar). All observations were taken in the B-configuration. Continuum observations were scheduled in $L$-band (1–2 GHz with the effective frequency (EF) of 1.4 GHz), $C$-band (4–8 GHz, EF 6 GHz) and $X$-band (8–12 GHz, EF 10 GHz) to be able to construct a radio spectral energy

[1] The physical properties and X-ray observations are discussed in Svoboda et al. (2019).

**Table 2.** VLA observation parameters for the sources with detections.

| Source | Time on source [min] | Effective frequency [GHz] | Total flux [μJy] | Beam size [″×″] |
|---|---|---|---|---|
| GP1 | 14.2 | 6.0 | 220 ± 6 | 1.0 × 0.9 |
| | 14.5 | 10.0 | 142 ± 10 | 0.6 × 0.6 |
| GP2 | 13.4 | 6.0 | 189 ± 11 | 1.2 × 0.9 |
| | 13.9 | 10.0 | 102 ± 9 | 0.6 × 0.5 |

**Notes.** The RMS noise in the images is ∼7 μJy beam$^{-1}$.

distribution (SED). Eight out of the scheduled nine blocks were observed, with ∼14 min on-source time and ∼30 min total time including calibration observations. 3C147 was used as a bandpass and amplitude calibrator, and J0741+3112 as the phase calibrator. The observations were performed with a short bandpass calibration scan at the beginning. The targets were observed for two sets of ∼7 min on-source, bracketed by phase calibration scans. The GP1 *L*-band observation was not completed during the observing period because of its low priority. The GP3 observations were performed with incorrect target coordinates, and therefore the source is outside the field of view for the *C*- and *X*-band observations, while it is still within the field of view in the *L*-band, but close to the edge of the primary beam, where the RMS noise is higher.

The data reduction and imaging were performed using the standard calibration pipeline with the Common Astronomy Software Applications (CASA v6.2.1, CASA Team et al. 2022) package. We used the multi-frequency synthesis and Briggs weighting with robust parameter = 0.5 for the imaging. The synthesised beam (angular resolution) in the B-configuration at *L*-, *C*- and *X*-bands is 4.3, 1.0 and 0.6 arcsec. The targets remain unresolved at this resolution. A summary of the observations with confirmed detections is provided in Table 2.

The radio images of the three GPs are shown in Fig. 1. Sources GP1 and GP2 are detected in both *C* and *X* bands and have comparable fluxes in the two bands. The RMS noise in these images is ∼7 μJy. The *L*-band observation of GP1 was not performed during the observation cycle, and the GP2 observation in the *L*-band is contaminated by artefacts from a particularly bright off-axis radio source. The radial streaks from the contaminating source pass close to the position of GP2, rendering it undetectable, and could not be mitigated by self-calibration. The source GP3 is within the field of view in the *L*-band, but there is no significant detection. The RMS noise near the source position is ∼70 μJy due to its location close to the edge of the field of view; thus the signal-to-noise ratio (S/N) is not sufficient to detect a ≤100 μJy source. In Table 2, we present the observation and source parameters for the detected sources (see Fig. 2).

### 2.2. Radio data from archival surveys

We supplement our targeted JVLA observations with the images from all-sky radio surveys with multiple instruments at different frequencies. We used the data from the TIFR GMRT Sky Survey (TGSS, Intema et al. 2017), an all-sky survey at 150 MHz with the Giant Metrewave Radio Telescope (GMRT); the VLA surveys, namely (1) the Faint Images of the Radio Sky at Twenty-centimeters (FIRST) Survey (White et al. 1997), (2) the NRAO VLA Sky Survey (NVSS, Condon et al. 1998) at 1.4 GHz, and (3) the VLA Sky Survey (VLASS, Gordon et al. 2021) at 3 GHz; the LOFAR Two-metre Sky Survey (LoTSS, Shimwell et al. 2022) with the Low Frequency Array at 150 MHz; and the Rapid ASKAP Continuum Survey first data release at 888 MHz (RACS, Hale et al. 2021), which provides a coverage for the sources in the southern sky. The properties of these surveys are provided in Table 3.

We searched the all-sky surveys mentioned in Table 3 to look for the detection of our GP sample at different frequencies in order to build their radio SEDs. In the archival data, GP1 was strongly detected in the LoTSS catalogue with a flux of 2.6 mJy, although it may also be affected by artefacts from a bright off-axis source. In the RACS and VLASS catalogues, GP1 was detected at 0.8 mJy and 0.54 mJy, respectively, but the detections are below the 5$\sigma$ limit of those surveys. GP1 is unresolved in all archival data, as the surveys lack the necessary resolution. GP2 and GP3 were undetected in all the survey catalogues. LoTSS, which has the best sensitivity among the aforementioned catalogues, currently does not have a sky coverage below a declination of +28° and thus has not yet observed GP2 and GP3, however it may be able to detect these sources and provide these in the future data releases.

A subsample of the Cardamone et al. (2009) GPs was observed by Chakraborti et al. (2012) with GMRT at 617 MHz. These authors observed three GP sources – including GP1 and GP2 – which were expected to have a ∼1 mJy flux at 617 MHz. The third source, J142405.73+421646.3, though different from our GP3, has similar galaxy stellar mass ($\log(M_\star/M_\odot) \sim 9$) and SFR ($19.6\,M_\odot\,\mathrm{yr}^{-1}$) and is located at a comparable redshift to that of GP3, of 0.18. Both GP1 and GP2 were detected at the 1 mJy level, while the third source was undetected, similar to GP3. In Table 4, we provide the detected flux densities of our targeted GPs in archival observations. The expected flux density ranges are estimated from the theoretical and empirical relations between SFR and radio luminosities (Eqs. (1)–(3), see Sect. 4 for details). The detections are consistent with the estimates from the SFR relations.

The detected fluxes of the two GPs were used to construct their radio SEDs, which are shown in Fig. 3. GP1 shows a standard power-law SED with the spectral index of $\alpha = -0.68 \pm 0.01$. GP2 shows an SED with a steeper power law with a spectral index of $\alpha = -0.95 \pm 0.17$. These spectral indices are characteristic of synchrotron emission, which can arise from star-forming activity as well as from accretion onto black holes (Panessa et al. 2019).

## 3. Comparison with the dwarf galaxy population

The detection of radio emission in two GP galaxies and the non-detection in one (or two, if we also include the third source from Chakraborti et al. 2012) raises the question of whether these detections are exceptional or representative of GP-like star-forming galaxies. In an attempt to provide an answer, we searched for radio counterparts for the GP and BB samples in the archival radio catalogues mentioned in Sect. 2. We cross-matched the GP sample from Cardamone et al. (2009) (80 star-forming and 8 narrow-line Seyfert 1 (NLS1) sources), along with the GPs from Keel et al. (2022) (38 sources) and Brunker et al. (2022) (13 sources) and the BB samples from Yang et al. (2017b) (40 sources), Jaskot et al. (2019) (13 sources) and McKinney et al. (2019) (17 sources). The radio catalogue images were further visually inspected to verify the detection (or the lack thereof).

A list of GP and BB sources with a radio counterpart detection is provided in Table 5. Older all-sky surveys, such as FIRST,

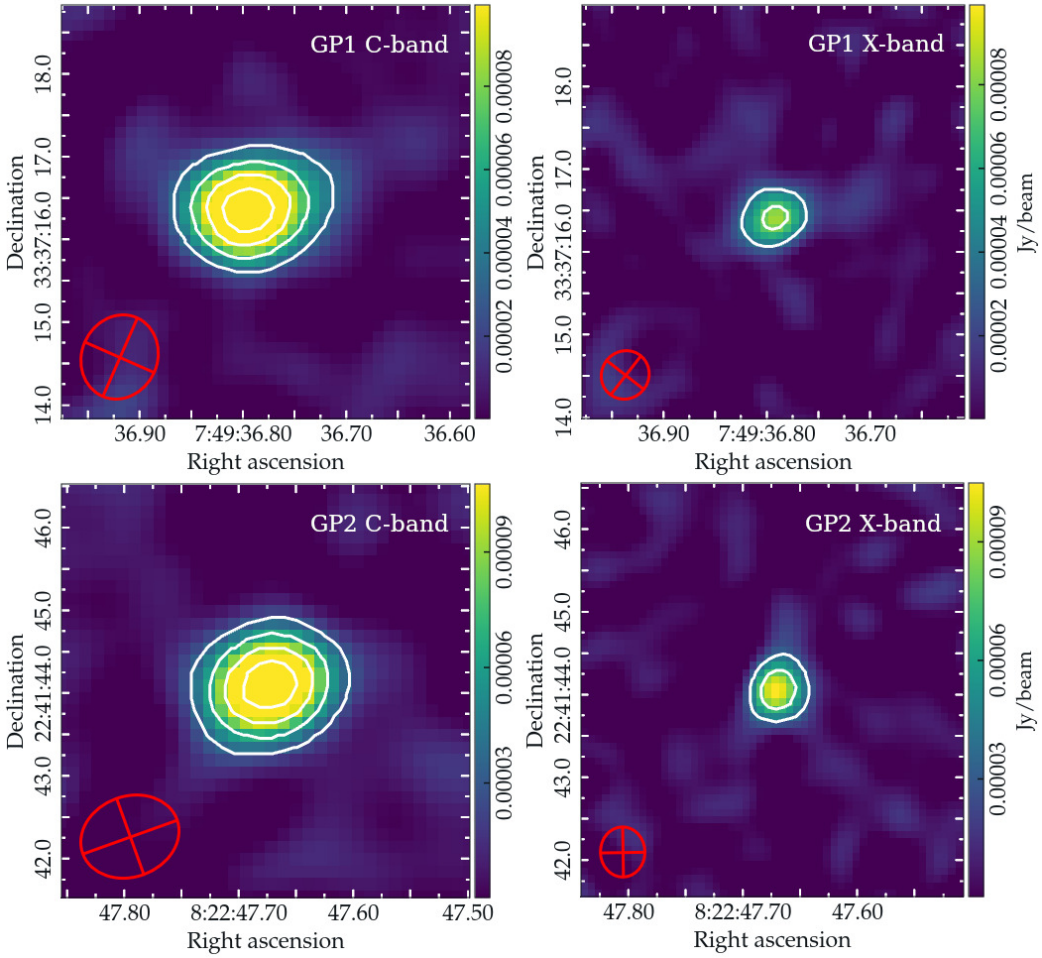


**Fig. 1.** Completed JVLA observations of the GPs showing detections of GP1 and GP2 in the *C*- and *X*-bands. The red ellipses in the bottom-left corner indicate the beam size and shape. The white contours represent $1\sigma \times (5, 9, 13, 17)$, where $1\sigma = 7\,\mu$Jy.

NVSS and TGSS, have significantly lower sensitivity and thus the GP and BB sources would not be detected in these surveys. None of the star-forming GP or BB sources were detected at $>5\sigma$ level in the VLASS or RACS surveys, which have slightly better sensitivity. For the LoTSS survey, the majority of the sources lie outside the current footprint and are not observed. Still, thanks to its excellent sensitivity and lower frequency where the sources are likely to be brighter, several sources are detected. In total, we detected 13 star-forming GPs from Cardamone et al. (2009), 8 from Brunker et al. (2022), 3 from Keel et al. (2022), 1 BB from Yang et al. (2017b) and 3 BBs from Jaskot et al. (2019).

However, 42 GPs and 17 BBs were observed within the LoTSS footprint without any detection, giving a detection rate of 35% and 17%, respectively. A subsample of 10 Yang et al. (2017b) BBs was observed by Sebastian & Bait (2019) using GMRT at 1.4 GHz, where they found nine out of ten detections. Most of the sources in their sample are considerably weak, with flux densities of $\leq$0.1 mJy. Only two sources have flux >0.1 mJy, one of which is within the LoTSS footprint, which is the only BB from Yang et al. (2017b) detected there. A simple two-point SED gives a very flat spectral index of $\alpha = -0.044$, which is often a characteristic of thermal free–free emission or free–free absorption, which trace the current star formation (Clemens et al. 2010).

Along with the star-forming GPs, Cardamone et al. (2009) also identified eight NLS1 galaxies, of which five were detected in LoTSS (and the other three are not observed), four in VLASS, and one in TGSS and NVSS. All the sources are detected with strong radio emission ranging from 2 to 400 mJy at low frequency (LoTSS and TGSS) and $\geq$1 mJy at high frequency in VLASS. Their radio spectral indices $\alpha$ lie between $-0.56$ and $-0.8$, which are typical for radio-loud AGNs. This is in contrast to the radio detections of star-forming GPs, where the total flux is $\leq$1 mJy at low frequency in LoTSS and is undetected in other surveys. The two exceptions to this are the following (1) Firstly, 195.36801+51.080893 (C09 26 in Table 5) is detected at 6.1 mJy and is considered a quasar candidate (Abazajian et al. 2009). The LoTSS image of this source shows an elongated radio structure which could be due to jet emission. This source is also close to (<25″) another strong radio source, and the radio emission associated with C09 26 may be contaminated by or associated with a radio jet from this nearby source. (2) The second exception is 117.403215+33.621219, also known as GP1 (C09 20 in Table 5), which is detected at 2.6 mJy. Similarly, one BB from the Jaskot et al. (2019) sample (J19 12 in Table 5) is detected in VLASS and FIRST at ∼1.2 mJy. This source is identified as an AGN candidate using a mid-IR colour cut (see Sartori et al. 2015; Comerford et al. 2020 for details). The source shows a change in flux between different VLASS epochs (1.6 mJy in epoch 1.1, 1.2 mJy in epoch 2.1 and 1.0 mJy in epoch 3.1), suggesting that it may be variable.

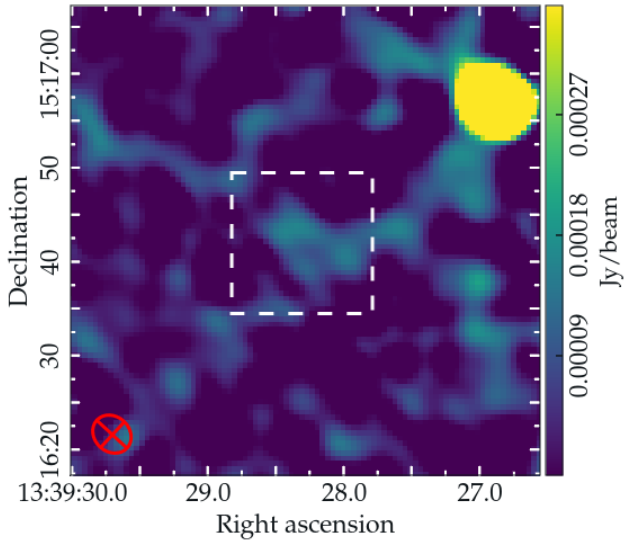


**Fig. 2.** Non-detection of the source GP3. The white dashed square is centred on the optical coordinates of the source and is $15 \times 15''$ in size. The red ellipse indicates the beam size and shape. The source is not detected because of its faintness and higher RMS noise in the image near the source coordinates.

**Table 3.** Summary of the archival radio surveys used for flux measurements of the targeted and archival sources.

| Survey | Observatory | Freq. [GHz] | Resolution [arcsec] | Sensitivity [mJy beam$^{-1}$] |
|---|---|---|---|---|
| FIRST | VLA | 1.4 | 5.4 | 0.15 [(a)] |
| NVSS | VLA | 1.4 | 45 | 0.45 [(a)] |
| VLASS | VLA | 3.0 | 2.5 | 0.145 |
| TGSS | GMRT | 0.15 | 25 | 5 |
| LoTSS | LOFAR | 0.15 | 6 | 0.083 |
| RACS | ASKAP | 0.888 | 15–25 | 0.2 |

**Notes.** [(a)]Although the median RMS noise is lower, the source-detection limit is $5 \times$ rms and the catalogues contain sources above this limit.

In summary, a typical star-forming GP or BB galaxy is likely radio-weak or undetected, and its low frequency flux is $\leq$1 mJy, while the galaxies hosting AGN or quasar candidates show strong radio emission and are detected in multiple surveys. With a strong radio detection at several radio frequencies, GP1 shows a closer similarity to the Seyfert galaxies than to the star-forming GPs, suggesting that it may host an AGN.

## 4. Star formation rate and radio flux relation

We tested whether the radio emission from the targeted GPs and archival sources is consistent with the expected emission from star formation, and investigated how many sources would be detectable with the archival surveys. The radio emission in star-forming galaxies arises from synchrotron emission from the relativistic electrons accelerated from supernova explosions interacting with the galactic magnetic field and from thermal bremsstrahlung (free–free) emission from ionised hydrogen gas surrounding hot young stars. At lower radio frequencies ($\leq$10 GHz), the synchrotron emission is dominant over the free–free emission (Condon 1992), and we can estimate the expected radio emission arising from SFR using only the synchrotron emission. Yun & Carilli (2002) provide a theoretical expected

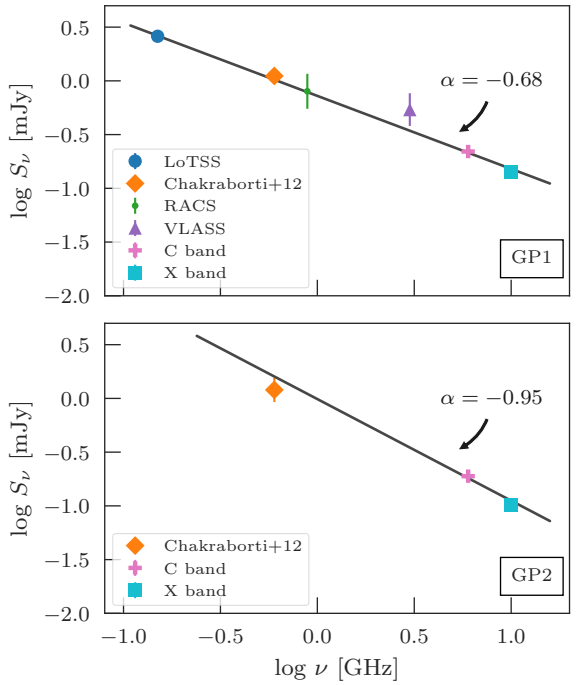


**Fig. 3.** Radio SED of GP1 and GP2. The data points are from the JVLA observations at 6 and 10 GHz, and archival measurements. GP2 shows a steeper spectral index compared to GP1. GP3 was not detected in any archival surveys.

non-thermal synchrotron flux density for a galaxy as

$$S(\nu) = 25 f_{nth} \nu^{\alpha}\ \mathrm{SFR}\ D_L^{-2}\ [\mathrm{Jy}] \quad (1)$$

where $\alpha$ is the synchrotron spectral index ($\sim$−0.7), $D_L$ is the luminosity distance in megaparsecs (Mpc), and $f_{nth}$ is a scaling factor introduced to account for the variations in normalisation. Table 1 in Yun & Carilli (2002) provides the $f_{nth}$ for some nearby galaxies, which are of the order $\sim$1. We take the mean of this distribution ($f_{nth} = 1.35$) as the value for our calculations, and use the standard deviation ($\sigma_f = 0.95$) as the error range.

For an empirical relation, Bell (2003) provide an estimation of SFR using far-IR and UV luminosities to calibrate the radio emission,

$$\mathrm{SFR} = 5.52 \times 10^{-22}\ L_{1.4\,\mathrm{GHz}} \quad (2)$$

for bright starburst galaxies. We invert this relation using the SFR obtained from UV-optical observations and use this to estimate the radio luminosity and, in turn, the radio flux density at 1.4 GHz, and extrapolate to different frequencies assuming $\alpha = -0.7$. Both Eqs. (1) and (2) were used to estimate the range of expected radio flux densities and the detectability of the sources at higher frequencies.

We detected the largest number of sources in the LoTSS survey. Most of the radio-to-SFR relations are calibrated to a frequency of 1.4 GHz or higher, and may not accurately reflect the expected flux at low frequency, that is, at 150 MHz. Thus, we used the relation between low-frequency radio flux and SFR derived for the LOFAR data, which is expressed as

$$\log(L_{150}) = a_1 \log(\mathrm{SFR}) + a_2 \quad (3)$$

where $L_{150}$ is the 150 MHz luminosity (in units of W Hz$^{-1}$) detected with LOFAR. Gürkan et al. (2018) used the SDSS-selected sample of 2000+ galaxies to study $L_{150}$−SFR relation,

**Table 4.** Archival detections of the targeted GPs with expected and observed flux densities in mJy.

| GP name | LoTSS [a] [0.15 GHz] | | GMRT [b] [0.62 GHz] | | RACS [c] [0.88 GHz] | | NVSS/FIRST [d] [1.4 GHz] | | VLASS [e] [3 GHz] | |
|---|---|---|---|---|---|---|---|---|---|---|
| | Exp. | Obs. | Exp. | Obs. | Exp. | Obs. | Exp. | Obs. | Exp. | Obs. |
| GP1 | 2.3–3.9 | 2.6 | 0.8–1.3 | 1.1 | 0.7–1.0 | 0.8 | 0.5–0.7 | <0.45 | 0.3–0.5 | 0.54 |
| GP2 | 2.4–4.1 | – | 0.9–1.5 | 1.2 | 0.7–1.1 | <0.2 | 0.5–0.8 | <0.45 | 0.3–0.5 | <0.15 |
| GP3 | 1.6–2.6 | – | 0.6–0.9 | – | 0.5–0.7 | <0.2 | 0.3–0.5 | <0.45 | 0.2–0.3 | <0.15 |

**Notes.** The expected fluxes are derived from Eqs. (1)–(3).
**References.** [a]LoTSS: Shimwell et al. (2022), [b]GMRT: Chakraborti et al. (2012), [c]RACS: Hale et al. (2021), [d]NVSS: Condon et al. (1998), FIRST: White et al. (1997), [e]VLASS: Gordon et al. (2021).

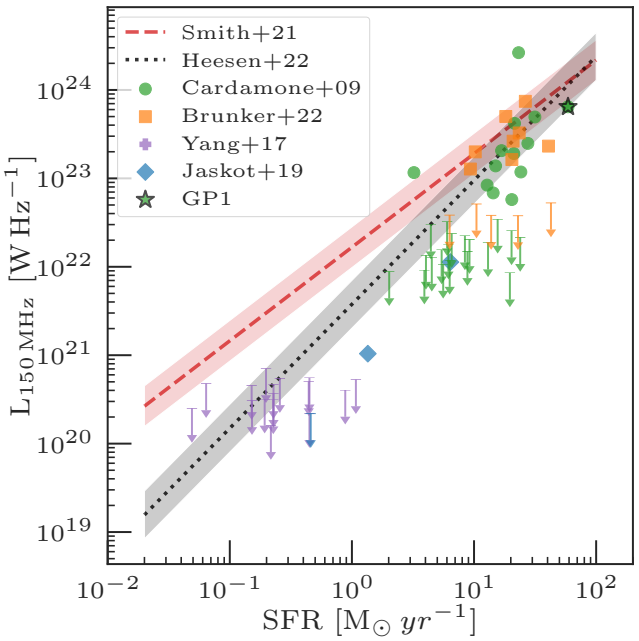


**Fig. 4.** Luminosities of the star-forming galaxies observed in the LoTSS survey at 150 MHz as a function of their SFR. The green circles and orange squares show the detected GPs while the purple crosses and blue diamonds show the detected BBs. The sources not detected in the LoTSS survey are shown by arrows as upper limits. The red dashed and the black dotted lines show the expected luminosity for a given SFR using the Smith et al. (2021) and Heesen et al. (2022) relations, respectively, and the shaded regions represent the scatter in the relations. The luminosities of most detected sources are either consistent or underluminous with respect to their SFR. All the undetected sources are significantly underluminous.

and find the best-fit values of $a_1 = 1.07 \pm 0.01$ and $a_2 = 22.06 \pm 0.01$, while Smith et al. (2021) used more than 100 000 near-IR-selected sources up to $z \sim 1$ and find similar values of $a_1 = 1.041 \pm 0.007$ and $a_2 = 22.181 \pm 0.005$. More recently, using 45 nearby galaxies (<30 Mpc), Heesen et al. (2022) found a steeper relation with $a_1 = 1.4 \pm 0.07$ and $a_2 = 21.57 \pm 0.04$. Using these relations, we calculate the expected luminosities for the GP and BB sources at 150 MHz.

The detected flux densities from GP1 and GP2 are overall consistent with the expectations from the SFR relation. As discussed in Sect. 3, most of the GPs and BBs appear to be radio-weak (≤1 mJy for the detected and <0.1 mJy for the undetected sources), thus it is useful to put the fluxes of our targeted GPs in this context and estimate their significance. Comparing the expected fluxes from the given SFR for the star-forming GPs and BBs at the different frequencies for respective catalogues, we find that none of the sources would be detectable at ≥5$\sigma$ level with the TGSS, FIRST, NVSS, or VLASS surveys. Two sources in this sample, namely GP1 and GP2, have the expected 3 GHz flux from Eqs. (1) and (2), which would be detectable with VLASS at 3$\sigma$ and 2$\sigma$ level, respectively. Following the Smith et al. (2021) relation (Eq. (3)), we expect ∼75% (70/93) of star-forming GPs and ∼83% of BBs (44/53) to be detectable at >5$\sigma$ level, but only 47% (21/45) of GPs and 10% (2/19) of BBs are actually detected. Similarly, the Heesen et al. (2022) relation predicts ∼57% (53/93) of GPs and ∼40% (21/53) of BBs could be detected. In Fig. 4, we plot the observed 150 MHz luminosities of the star-forming GPs and BBs as a function of their SFR, together with the expected luminosity following the Smith et al. (2021) relation (red dashed line), and the Heesen et al. (2022) relation (black dotted line). The GPs that have been detected lie on the relations within the error margin, or are below the relation by a factor of a few. One exception to this is the quasar candidate (C09 26/K22 20 in Table 5), which is overluminous by a factor of ∼7. The source GP1 has a 150 MHz luminosity that is approximately the same as expected from the SFR. The high radio flux detected for GP1 compared to the rest of the GP sample is likely due to its high SFR, which is the highest SFR among all GPs and BBs considered in this work. The two detected BBs are below the Smith et al. (2021) relation by an order of magnitude. All the undetected sources are also well below this relation. The steeper $L_{150}$−SFR relation by Heesen et al. (2022) reduces the discrepancy between the observed and the expected luminosities but the two detected BBs and the undetected sources are below the relation by a factor of a few. The Gürkan et al. (2018) and Smith et al. (2021) relations are based on statistically significant large samples up to $z \leq 1$ spanning a wide range of galaxy SFRs that are representative of the GP and BB galaxies. The galaxies in the Heesen et al. (2022) sample are much closer ($z < 0.01$) and thus weaker sources are easier to detect, which could steepen the relation. All three relations are based on galaxies with larger stellar masses ($\log(M_\star/M_\odot) \geq 8.5$), which cover the GP mass range, but are more massive than the BBs ($\log(M_\star/M_\odot) \approx 6$–$8$). Gürkan et al. (2018) and Smith et al. (2021) suggest that the $L_{150}$−SFR also depends on the galaxy stellar mass: $\log(L_{150}) = a_1 \log(\mathrm{SFR}) + a_2 \log(M_\star) + a_3$. Using the values for the coefficients $a_1$, $a_2$, and $a_3$ provided by these latter authors, we compare the estimated and observed luminosity. The observed luminosities of the detected GPs are consistent with or higher than expected luminosities, while the detected BB and the undetected sources have observed luminosities that are below expectation by a factor of a few. Thus, even accounting for the mass dependence, lower-mass galaxies appear underluminous. Our analysis suggests that the $L_{150}$−SFR relation is

**Table 5.** Radio-detected archival GP and BB galaxies.

| Source id | RA [h:m:s] | Dec [d:m:s] | $z$ | LoTSS [mJy] | TGSS [mJy] | NVSS [mJy] | FIRST [mJy] | VLASS [mJy] | Classification |
|---|---|---|---|---|---|---|---|---|---|
| C09 15 | 14:11:45.327 | +62:39:11.212 | 0.2301 | 0.5 | – | – | – | – | SF |
| C09 17 | 15:40:50.206 | +57:24:41.935 | 0.2944 | 0.7 | – | – | – | – | SF |
| C09 20 | 07:49:36.773 | +33:37:16.395 | 0.2733 | 2.6 | – | – | – | 0.54 | SF (†) |
| C09 25 | 09:26:00.403 | +44:27:36.171 | 0.1807 | 0.7 | – | – | – | – | SF |
| C09 26 | 13:01:28.312 | +51:04:51.200 | 0.3479 | 6.1 | – | – | – | 0.7 | QC (‡) |
| C09 31 | 10:53:30.815 | +52:37:52.858 | 0.2526 | 1.2 | – | – | – | – | SF |
| C09 32 | 08:47:54.082 | +33:36:54.646 | 0.3063 | 1.3 | – | – | – | – | SF |
| C09 33 | 13:39:40.709 | +55:27:40.100 | 0.2291 | 0.7 | – | – | – | – | SF |
| C09 44 | 09:57:39.774 | +37:42:07.581 | 0.2867 | 0.5 | – | – | – | – | SF |
| C09 45 | 14:40:09.956 | +46:19:36.970 | 0.3008 | 1.6 | – | – | – | – | SF |
| C09 46 | 14:54:35.581 | +45:28:56.248 | 0.2687 | 0.8 | – | – | – | – | SF |
| C09 58 | 11:37:22.138 | +35:24:26.623 | 0.1945 | 0.5 | – | – | – | – | SF |
| C09 59 | 11:26:37.771 | +38:03:03.062 | 0.2469 | 0.5 | – | – | – | – | SF |
| C09 N2 | 14:19:18.900 | +51:02:40.142 | 0.3236 | 6.8 | – | – | 1.45 | 1.4 | NLS1 |
| C09 N3 | 16:22:09.407 | +35:21:07.269 | 0.2660 | 13.2 | – | – | 2.0 | 1.8 | NLS1 |
| C09 N4 | 07:49:32.947 | +28:34:06.750 | 0.3369 | 342 | 390 | 27 | 28 | 10.2 | NLS1 |
| C09 N5 | 11:29:07.104 | +57:56:05.206 | 0.3123 | 11.4 | – | – | 1.92 | 1.8 | NLS1 |
| C09 N6 | 11:26:15.265 | +38:58:17.389 | 0.3365 | 2.2 | – | – | 1.2 | – | NLS1 |
| C09 N7 | 08:18:00.198 | +19:18:10.181 | 0.3245 | – (*) | – | – | 1.4 | 0.93 | NLS1 |
| K22 1 | 15:04:57.987 | +59:54:07.27 | 0.2502 | 0.6 | – | – | – | – | SF |
| K22 4 | 14:10:05.248 | +53:50:37.89 | 0.3353 | 0.5 | – | – | – | – | SF |
| K22 20 | 13:01:28.316 | +51:04:51.18 | 0.3479 | 6.1 | – | – | – | 0.7 | QC (‡) |
| B22 1 | 13:10:09.40 | +29:17:42.9 | 0.3582 | 0.5 | – | – | – | – | SF |
| B22 5 | 12:22:24.2 | +43:11:23.0 | 0.3049 | 0.4 | – | – | – | – | SF |
| B22 6 | 13:14:41.28 | +43:43:26.5 | 0.2939 | 0.68 | – | – | – | – | SF |
| B22 7 | 13:15:49.44 | +43:34:30.4 | 0.3276 | 0.7 | – | – | – | – | SF |
| B22 9 | 14:29:40.9 | +43:54:09.0 | 0.3592 | 0.7 | – | – | – | – | SF |
| B22 10 | 14:36:20.3 | +43:53:02.0 | 0.3311 | 1.3 | – | – | – | – | SF |
| B22 11 | 15:26:23.8 | +43:00:16.45 | 0.3688 | 1.5 | – | – | – | – | SF |
| B22 12 | 15:42:46.5 | +43:53:58.20 | 0.3080 | 0.5 | – | – | – | – | SF |
| Y17 8 | 15:09:34.174 | +37:31:46.12 | 0.0326 | 0.4 | – | – | – | – | SF (§) |
| J19 4 | 08:51:15.655 | +58:40:54.997 | 0.0919 | 0.5 | – | – | – | – | SF |
| J19 10 | 15:09:34.174 | +37:31:46.12 | 0.0325 | 0.4 | – | – | – | – | SF (§) |
| J19 12 | 17:35:01.229 | +57:03:08.458 | 0.0472 | – (*) | – | – | 1.3 | 1.2 | AGN |

**Notes.** (*): Not observed; SF = star forming; QC = quasar candidate (Abazajian et al. 2009); NLS1 = narrow line Seyfert 1; AGN = AGN candidate (Sartori et al. 2015). (†): GP1; (‡): C09 26 same as K22 20; (§): Y17 8 same as J19 10.
**References.** C09: Cardamone et al. (2009), K22: Keel et al. (2022), B22: Brunker et al. (2022), Y17: Yang et al. (2017b), J19: Jaskot et al. (2019).

possibly even steeper towards the lower-mass end, and a careful analysis using a sample consisting of low-mass galaxies is needed to establish accurate relations spanning the whole galaxy mass range.

## 5. Conclusions and discussion

In this paper, we present the JVLA observations of three GP galaxies.

1. JVLA observations: GP1 and GP2 are clearly detected in *C*- and *X*-band observations. A GP1 *L*-band observation was not performed and the GP2 *L*-band image is affected by artefacts from a nearby bright source. GP3 was undetected in the *L*-band observations, while it is outside the field of view in the *C*- and *X*-band images.
2. Archival observations: We supplemented our JVLA observations with archival radio surveys to construct radio SEDs for GP1 and GP2. The detected radio fluxes of the two sources are consistent with the expected radio emission from star formation. GP3 is not detected in any of the considered archival surveys.
3. Supplementary sample: We compare our observations with a larger sample of GPs and BBs in the archival surveys and in the literature to understand the nature of radio emission in dwarf star-forming galaxies. We find that only a small fraction (36%) of GPs and BBs are detected in the archives. On the other hand, dwarf galaxies that have been classified as AGNs or AGN candidates show strong radio emission and are often detected in several archival surveys.
4. Radio flux−SFR relation: We compared the detected radio luminosity of the star-forming galaxies with the luminosity expected from SFR derived from empirical relations. Although about 55–75% of sources could be detected with the most sensitive LoTSS survey, fewer than 40% are detected. A few of the detected and most of the undetected

sources are underluminous compared to expectations from the empirical relations. This suggests that towards the lower end of the galaxy mass and SFR, the radio-flux-to-SFR relation deviates away from the relations established for larger galaxies. Typical compact, highly star-forming dwarf galaxies, such as GPs and BBs are markedly underluminous, and the presence of strong radio emission may hint at an alternative source such as an AGN.

Such a deficiency in the radio flux of GPs and BBs has been reported before. Chakraborti et al. (2012) showed that GPs have lower radio flux in comparison with local starburst galaxies and expectations from empirical relations. Sebastian & Bait (2019) show that the radio-derived SFR is significantly lower than the H$\alpha$-derived SFR. The radio flux in the star-forming galaxies likely depends on the galaxy mass, as Kouroumpatzakis et al. (2021) showed that there is a significant deficit in radio luminosity compared to H$\alpha$ luminosity for low-mass galaxies. GPs and BBs, with $\log(M_\star/M_\odot) \sim 9$ and $\log(M_\star/M_\odot) \sim 7$, respectively, are on the lower end of the mass range and show a similar trend. Our analysis with a large sample of low-mass, high-SFR galaxies confirms that they do not follow the same relation as high-mass galaxies.

The radio and IR emission in star-forming galaxies is often described by the "calorimeter" model (Voelk 1989). The energy from UV photons is completely reprocessed by the dust in the galaxy and radiated in the far-IR, while the energy from electrons driven by supernova explosions is extracted entirely as synchrotron emission before they escape the galaxy. Thus, the galaxies behave as both UV and electron calorimeters. Several studies have now shown that towards the low-mass end, galaxies may not act as perfect calorimeters and both the radio and IR emission is suppressed (Bell 2003; Boyle et al. 2007; Beswick et al. 2008; Roychowdhury & Chengalur 2012; Smith et al. 2021; Heesen et al. 2022; Kouroumpatzakis et al. 2023), as the dust content and the efficiency of synchrotron emission is reduced by a similar factor (Lacki et al. 2010; Lacki & Thompson 2010). Our analysis demonstrates that towards the lowest end of galaxy mass and SFR, the radio emission deviates from the radio–SFR relation established for more massive galaxies, supporting the findings of the above studies. This could be due to a higher escape fraction of synchrotron-emitting electrons due to a weaker gravitational potential of the low-mass galaxies. Dwarf galaxies also do not show settled morphology, and consequently they may not host large-scale and high-intensity magnetic fields.

The radio observations of the three targeted GPs show similarities with their X-ray observations, where GP1 and GP2 were detected in the X-rays with more than five times excess flux compared to what is expected from SFR relations, while GP3 remained undetected (Svoboda et al. 2019). This X-ray excess cannot be explained by a higher number of high-mass X-ray binaries or excess emission from the hot gas (Franeck et al. 2022) and is often attributed to the presence of an AGN. The X-ray and radio emission could arise from the same source, which is different from the emission in the optical band. A systematic comparison of the multi-wavelength properties of star-forming dwarf galaxies is necessary to understand the cause of the emission (or the lack of detectable emission) and the relation between the radio and X-ray regimes, and how the radio and X-ray properties differ from the optical and IR properties. Surveys from recently launched and next-generation of observatories (e.g JWST, *Euclid, Athena*, the Square Kilometre Array, *Vera C. Rubin* Observatory etc.) will be able to access the areas of parameter space occupied by lower-mass and dwarf galaxies, even at higher redshift. Thus, it is crucial to understand how the luminosity–SFR relations hold for the low-mass galaxies with a diverse range of SFRs and cosmic ages.

*Acknowledgements.* We thank the anonymous referee for their helpful comments which helped to improve the manuscript. This work was supported from the Czech Science Foundation project No. 22-22643S. B.M. acknowledges support from the Science and Technology Facilities Council (STFC) under grants ST/T000295/1 and ST/X001164/1. This publication makes use of data products from NSF's *Karl G. Jansky* Very Large Array (VLA). The National Radio Astronomy Observatory is a facility of the National Science Foundation operated under cooperative agreement by Associated Universities, Inc. This research has made use of the CIRADA cutout service at `http://cutouts.cirada.ca`, operated by the Canadian Initiative for Radio Astronomy Data Analysis (CIRADA). CIRADA is funded by a grant from the Canada Foundation for Innovation 2017 Innovation Fund (Project 35999), as well as by the Provinces of Ontario, British Columbia, Alberta, Manitoba and Quebec, in collaboration with the National Research Council of Canada, the US National Radio Astronomy Observatory and Australia's Commonwealth Scientific and Industrial Research Organisation. This research has made use of ESASky (Baines et al. 2017; Giordano et al. 2018), developed by the ESAC Science Data Centre (ESDC) team and maintained alongside other ESA science mission's archives at ESA's European Space Astronomy Centre (ESAC, Madrid, Spain). This research has made use of the SIMBAD database, operated at CDS, Strasbourg, France (Wenger et al. 2000). Software used: `Numpy` (Harris et al. 2020), `matplotlib` (Hunter 2007), `astropy` (Astropy Collaboration 2013, 2018, 2022), `CARTA` (Comrie et al. 2021).

## References

Abazajian, K. N., Adelman-McCarthy, J. K., Agüeros, M. A., et al. 2009, ApJS, 182, 543
Adams, N. J., Conselice, C. J., Ferreira, L., et al. 2023, MNRAS, 518, 4755
Astropy Collaboration (Robitaille, T. P., et al.) 2013, A&A, 558, A33
Astropy Collaboration (Price-Whelan, A. M., et al.) 2018, AJ, 156, 123
Astropy Collaboration (Price-Whelan, A. M., et al.) 2022, ApJ, 935, 167
Atek, H., Chemerynska, I., Wang, B., et al. 2023a, MNRAS, 524, 5486
Atek, H., Shuntov, M., Furtak, L. J., et al. 2023b, MNRAS, 519, 1201
Baines, D., Giordano, F., Racero, E., et al. 2017, PASP, 129, 028001
Baldwin, J. A., Phillips, M. M., & Terlevich, R. 1981, PASP, 93, 5
Bell, E. F. 2003, ApJ, 586, 794
Best, P. N., & Heckman, T. M. 2012, MNRAS, 421, 1569
Beswick, R. J., Muxlow, T. W. B., Thrall, H., Richards, A. M. S., & Garrington, S. T. 2008, MNRAS, 385, 1143
Bogdán, Á., Goulding, A. D., Natarajan, P., et al. 2024, Nat. Astron., 8, 126
Bouwens, R. J., Illingworth, G. D., Oesch, P. A., et al. 2015, ApJ, 811, 140
Boyle, B. J., Cornwell, T. J., Middelberg, E., et al. 2007, MNRAS, 376, 1182
Brunker, S. W., Salzer, J. J., Kimsey-Miller, B., & Cousins, B. 2022, ApJ, 926, 131
Cardamone, C., Schawinski, K., Sarzi, M., et al. 2009, MNRAS, 399, 1191
CASA Team, Bean, B., Bhatnagar, S., et al. 2022, PASP, 134, 114501
Castellano, M., Fontana, A., Treu, T., et al. 2022, ApJ, 938, L15
Chakraborti, S., Yadav, N., Cardamone, C., & Ray, A. 2012, ApJ, 746, L6
Clemens, M. S., Scaife, A., Vega, O., & Bressan, A. 2010, MNRAS, 405, 887
Cole, S., Lacey, C. G., Baugh, C. M., & Frenk, C. S. 2000, MNRAS, 319, 168
Comerford, J. M., Negus, J., Müller-Sánchez, F., et al. 2020, ApJ, 901, 159
Comrie, A., Wang, K.-S., Hsu, S.-C., et al. 2021, `https://doi.org/10.5281/zenodo.4905459`
Condon, J. J. 1992, ARA&A, 30, 575
Condon, J. J., Cotton, W. D., Greisen, E. W., et al. 1998, AJ, 115, 1693
Finkelstein, S. L., Bagley, M. B., Arrabal Haro, P., et al. 2022, ApJ, 940, L55
Franeck, A., Wünsch, R., Martínez-González, S., et al. 2022, ApJ, 927, 212
Giallongo, E., Grazian, A., Fiore, F., et al. 2015, A&A, 578, A83
Giordano, F., Racero, E., Norman, H., et al. 2018, Astron. Comput., 24, 97
Gordon, Y. A., Boyce, M. M., O'Dea, C. P., et al. 2021, ApJS, 255, 30
Goulding, A. D., Greene, J. E., Setton, D. J., et al. 2023, ApJ, 955, L24
Gürkan, G., Hardcastle, M. J., Smith, D. J. B., et al. 2018, MNRAS, 475, 3010
Hale, C. L., McConnell, D., Thomson, A. J. M., et al. 2021, PASA, 38, e058
Harris, C. R., Millman, K. J., van der Walt, S. J., et al. 2020, Nature, 585, 357
Hayes, M. 2015, PASA, 32, e027
Heesen, V., Staffehl, M., Basu, A., et al. 2022, A&A, 664, A83
Hunter, J. D. 2007, Comput. Sci. Eng., 9, 90
Intema, H. T., Jagannathan, P., Mooley, K. P., & Frail, D. A. 2017, A&A, 598, A78
Jaskot, A. E., Dowd, T., Oey, M. S., Scarlata, C., & McKinney, J. 2019, ApJ, 885, 96

Juodžbalis, I., Conselice, C. J., Singh, M., et al. 2023, MNRAS, 525, 1353
Kaviraj, S., Martin, G., & Silk, J. 2019, MNRAS, 489, L12
Keel, W. C., Tate, J., Wong, O. I., et al. 2022, AJ, 163, 150
Körding, E. G., Jester, S., & Fender, R. 2006, MNRAS, 372, 1366
Kouroumpatzakis, K., Zezas, A., Maragkoudakis, A., et al. 2021, MNRAS, 506, 3079
Kouroumpatzakis, K., Zezas, A., Kyritsis, E., Salim, S., & Svoboda, J. 2023, A&A, 673, A16
Labbé, I., van Dokkum, P., Nelson, E., et al. 2023, Nature, 616, 266
Lacki, B. C., & Thompson, T. A. 2010, ApJ, 717, 196
Lacki, B. C., Thompson, T. A., & Quataert, E. 2010, ApJ, 717, 1
Latimer, L. J., Reines, A. E., Plotkin, R. M., Russell, T. D., & Condon, J. J. 2019, ApJ, 884, 78
Loeb, A., & Barkana, R. 2001, ARA&A, 39, 19
McKinney, J. H., Jaskot, A. E., Oey, M. S., et al. 2019, ApJ, 874, 52
Mezcua, M., Suh, H., & Civano, F. 2019, MNRAS, 488, 685
Miller, B. P., Gallo, E., Greene, J. E., et al. 2015, ApJ, 799, 98
Moravec, E., Svoboda, J., Borkar, A., et al. 2022, A&A, 662, A28
Naidu, R. P., Oesch, P. A., van Dokkum, P., et al. 2022, ApJ, 940, L14
Nyland, K., Marvil, J., Wrobel, J. M., Young, L. M., & Zauderer, B. A. 2012, ApJ, 753, 103
Panessa, F., Baldi, R. D., Laor, A., et al. 2019, Nat. Astron., 3, 387
Planck Collaboration VI. 2020, A&A, 641, A6
Reines, A. E. 2022, Nat. Astron., 6, 26
Reines, A. E., Plotkin, R. M., Russell, T. D., et al. 2014, ApJ, 787, L30
Reines, A. E., Condon, J. J., Darling, J., & Greene, J. E. 2020, ApJ, 888, 36
Rhoads, J. E., Wold, I. G. B., Harish, S., et al. 2023, ApJ, 942, L14
Robertson, B. E., Ellis, R. S., Furlanetto, S. R., & Dunlop, J. S. 2015, ApJ, 802, L19
Roychowdhury, S., & Chengalur, J. N. 2012, MNRAS, 423, L127
Sartori, L. F., Schawinski, K., Treister, E., et al. 2015, MNRAS, 454, 3722
Schaerer, D., Marques-Chaves, R., Barrufet, L., et al. 2022, A&A, 665, L4
Sebastian, B., & Bait, O. 2019, ApJ, 882, L19
Shapiro, P. R., & Giroux, M. L. 1987, ApJ, 321, L107
Shimwell, T. W., Hardcastle, M. J., Tasse, C., et al. 2022, A&A, 659, A1
Smith, D. J. B., Haskell, P., Gürkan, G., et al. 2021, A&A, 648, A6
Steidel, C. C., Pettini, M., & Adelberger, K. L. 2001, ApJ, 546, 665
Svoboda, J., Douna, V., Orlitová, I., & Ehle, M. 2019, ApJ, 880, 144
Voelk, H. J. 1989, A&A, 218, 67
Volonteri, M., & Gnedin, N. Y. 2009, ApJ, 703, 2113
Wenger, M., Ochsenbein, F., Egret, D., et al. 2000, A&AS, 143, 9
White, R. L., Becker, R. H., Helfand, D. J., & Gregg, M. D. 1997, ApJ, 475, 479
Yang, H., Malhotra, S., Gronke, M., et al. 2017a, ApJ, 844, 171
Yang, H., Malhotra, S., Rhoads, J. E., & Wang, J. 2017b, ApJ, 847, 38
Yun, M. S., & Carilli, C. L. 2002, ApJ, 568, 88